The dominant role of semi-arid ecosystems in the trend and variability of the land CO2 sink

Ahlström, Anders; Raupach, Michael R.; Schurgers, Guy; Smith, Benjamin; Arneth, Almut; Jung, Martin; Reichstein, Markus; Canadell, Josep G.; Friedlingstein, Pierre; Jain, Atul K.; Kato, Etsushi; Poulter, Benjamin; Sitch, Stephen; Stocker, Benjamin D.; Viovy, Nicolas; Wang, Ying Ping; Wiltshire, Andy; Zaehle, Sönke; Zeng, Ning

Published in:
Science

DOI:
10.1126/science.aaa1668

2015

The dominant role of semi-arid ecosystems in the trend and variability of the land CO_2 sink

Authors: Anders Ahlström[1,2*], Michael R. Raupach[3], Guy Schurgers[4], Benjamin Smith[1], Almut Arneth[5], Martin Jung[6], Markus Reichstein[6], Josep G. Canadell[7], Pierre Friedlingstein[8], Atul K. Jain[9], Etsushi Kato[10], Benjamin Poulter[11], Stephen Sitch[12], Benjamin D. Stocker[13,14], Nicolas Viovy[15], Ying Ping Wang[16], Andy Wiltshire[17], Sönke Zaehle[6], Ning Zeng[18]

Affiliations:

[1]Lund University, Department of Physical Geography and Ecosystem Science, 223 62 Lund, Sweden.

[2]Department of Earth System Science, School of Earth, Energy and Environmental Sciences, Stanford University, Stanford, CA 94305, USA

[3]Australian National University, Climate Change Institute, Canberra, ACT 0200, Australia.

[4]Department of Geosciences and Natural Resource Management, University of Copenhagen, 1350 Copenhagen, Denmark.

[5]Karlsruhe Institute for Technology, Institute for Meteorology and Climate Research-Atmospheric Environmental Research, 82476 Garmisch-Partenkirchen, Germany.

[6]Max Planck Institute for Biogeochemistry, 07745 Jena, Germany.

[7]Global Carbon Project, CSIRO Oceans and Atmospheric Flagship, Canberra, Australian Capital Territory, Australia

[8]College of Engineering, Mathematics and Physical Sciences, University of Exeter, Exeter EX4 4QF, UK.

[9]Department of Atmospheric Sciences, University of Illinois, Urbana-Champaign, 105 S. Gregory Street, Urbana, IL 61801.

[10]The Institute of Applied Energy, 105-0003, Tokyo, Japan.

[11]Montana State University, Institute on Ecosystems and the Department of Ecology, Bozeman,Montana 59717, USA.

[12]College of Life and Environmental Sciences, University of Exeter, Exeter EX4 4RJ, UK.

[13]Department of Life Sciences, Imperial College, Silwood Park, Ascot SL5 7PY, UK.

[14]Climate and Environmental Physics, Physics Institute and Oeschger Centre for Climate Change Research, University of Bern, Bern, Switzerland.

[15]Laboratoire des sciences du climat et de l'environnement, Bat 712, Orme des Merisiers, CEA Saclay, F-91191 Gif sur Yvette CEDEX. France.

[16]CSIRO Ocean and Atmosphere Flagship, PMB 1, Aspendale Vic 3195, Australia.

[17]Met Office Hadley Centre, Fitzroy Road, Exeter, Devon, Ex1 3PB, UK.

[18]Department of Atmospheric and Oceanic Science and Earth System Science Interdisciplinary Center, University of Maryland, College Park, MD 20742-2425, USA.

*Correspondence to: anders.ahlstrom@nateko.lu.se

Abstract:

The growth rate of atmospheric CO_2 concentrations since industrialization is characterized by large interannual variability, mostly resulting from variability in the CO_2 uptake by terrestrial ecosystems. However, the contributions of regional ecosystems to that variability are not well known. Using an ensemble of ecosystem and land-surface models and an empirical observation-based product of the global gross primary production, we show that the mean sink, trend, and interannual variability in CO_2 uptake by terrestrial ecosystems are dominated by distinct biogeographic regions. Whereas the sink strength is dominated by highly productive lands, mainly tropical forests, the trend and interannual variability of the sink are dominated by semi-arid ecosystems whose carbon balance is strongly associated with circulation-driven variations in both precipitation and temperature.

One Sentence Summary:

Semi-arid savannas and shrub lands dominate the trend and interannual variability of the global land CO_2 sink.

Main Text:

Since the 1960s, terrestrial ecosystems have acted as a substantial sink for atmospheric CO_2, sequestering about one quarter of anthropogenic emissions in an average year (*1*). This ecosystem service, which helps mitigate climate change by reducing the rate of increase of atmospheric greenhouse gases, is due to an imbalance between the uptake of CO_2 through gross primary production (GPP, the aggregate photosynthesis of plants) and the release of carbon to the atmosphere by ecosystem respiration (R_{eco}) and other losses, including wildfires (C_{fire}). The net carbon flux (net biome production, NBP = GPP - R_{eco} - C_{fire}) results from the small imbalance between the much larger uptake and release fluxes. Consequently, small fractional variations in either of these fluxes can cause substantial absolute variations in net carbon exchange with the atmosphere. These variations account almost entirely for year-to-year variations around the overall trend in atmospheric concentrations of CO_2 (*2, 3*).

Modelling studies suggest a large uncertainty of the future magnitude and sign of the carbon sink provided by terrestrial ecosystems (*4-8*). Robust projections are crucial to assess future atmospheric CO_2 burdens and associated climate change, and also for developing effective mitigation policies. Reducing uncertainty requires better knowledge of the regions and processes governing the present sink and its variations. Inventories suggest that the majority of carbon sequestered by the terrestrial biosphere since industrialization has accumulated in forest ecosystems of the tropics and temperate zones (*9*). However, the relative contributions of ecosystems of different, climatically-distinct, regions to variations in the land sink on interannual to multi-decadal time scales are not well characterized. Here we investigate relative regional contributions to, respectively, the mean sink, its trend over recent decades and the interannual variability (IAV) around the trend.

We simulate the geographic pattern and time course of NBP using LPJ-GUESS (*10-12*), a biogeochemical dynamic global vegetation model (DGVM) that explicitly accounts for the dependency of plant production and downstream ecosystem processes on the demography (size structure) and composition of simulated vegetation. We force the model with historical climate (*13*) and CO_2 concentrations, accounting for emissions from land use change and carbon uptake due to regrowth following agricultural abandonment (*14*). We compare the results to an ensemble of nine ecosystem and land surface model simulations from the TRENDY model intercomparison project (*12, 15*) (hereinafter TRENDY models, Table S1). The TRENDY ensemble is similarly based on historical climate and CO_2, but employs a static 1860 land use mask.

Global NBP as simulated by LPJ-GUESS shows strong agreement (r^2=0.62) with the Global Carbon Project (GCP) estimate of the net land CO_2 flux; an independent, bookkeeping-based estimate derived as the residual of emissions, atmospheric growth and ocean uptake of CO_2 (*1*) (Fig 1A). TRENDY models do not account for land use change. In comparison to the GCP land flux estimate they consequently predict a higher average NBP but similar interannual variation. Moreover, the offset between the TRENDY ensemble mean and the GCP land flux estimate is comparable to the GCP estimate of mean land use change emissions for the period 1982-2011 (fLUC).

We divide the global land area into six land cover classes following the MODIS MCD12C1 land cover classification (*12, 16*): tropical forests (Fig 1B), extra-tropical forest, grasslands and croplands (here combined), semi-arid ecosystems (Fig 1C), tundra and arctic shrub lands, and sparsely vegetated lands (areas classified as barren) (Fig S1 and S2).

When the global terrestrial CO_2 sink (average NBP) and its trend (1982-2011) are partitioned among land cover classes, we find that tropical forests account for the largest fraction (26%, 0.33 PgC $year^{-1}$) of the average sink over this period (1.23 PgC $year^{-1}$) (Fig. 1D). In contrast, we find that semi-arid ecosystems dominate the positive global CO_2 sink trend (57%, 0.04 PgC $year^{-2}$, global: 0.07 PgC $year^{-2}$) (Fig. 1E). The TRENDY ensemble shows a consistent pattern, with tropical forests dominating the mean sink (median: 24%) and semi-arid ecosystems dominating the trend (median: 51%). The predominance of semi-arid ecosystems in explaining the global land sink trend is consistent with widespread observations of woody encroachment over semi-arid areas (*17*) and increased vegetation greenness inferred from satellite remote sensing over recent decades (*17-19*). Likewise, a recent study attributes the majority of the record land sink anomaly of 2011 to the response of semi-arid ecosystems in the Southern Hemisphere, particularly Australia, to an anomalous wet period; the study further postulates a recent increase in the sensitivity of carbon uptake to precipitation for this region due to vegetation expansion (*20*).

We further partition interannual variability in global NBP among land cover classes based on the contribution of individual grid cells to global NBP IAV (*12*). To this end, we adopted an index (Eq. S1, Fig S3) that scores individual geographic locations according to the consistency over time (years) with which the local NBP flux resembles the sign and magnitude of global NBP (Fig S4). Regions receiving higher and positive average scores are inferred to have a larger contribution in governing global NBP IAV, as opposed to regions characterized by smaller or negative (counteracting) scores (Fig S3). The index we adopt does not characterize the *variability* of ecosystems of different land cover classes as, for example

the standard deviation would do (Fig S5) but rather enables a comparison of their relative importance (contribution) in governing global IAV.

Semi-arid ecosystems were found to account for the largest fraction, 39%, of global NBP IAV, exceeding tropical forest (19%), extra-tropical forest (11%; all forest: 30%) and grasslands and croplands (27%) (Fig 1F). The TRENDY ensemble shows a similar partitioning, with semi-arid ecosystems accounting for 47% (median; tropical forests: 28%, extra-tropical forest: 6%, all forest: 35%). The overall contributions per land cover class are the sum of both positive and negative contributions that result from differences in phase between IAV of individual grid cells compared with global IAV (Fig S4). The extent to which negative contributions reduce the overall land cover class contributions is minor for all regions except grasslands and crops (Fig S6) (LPJ-GUESS: -13%, TRENDY median: -13%) the latter being distributed widely across climate zones, both climate variations and the sensitivity of NBP to climate variations differing among regions.

To partition the global NBP IAV among component fluxes (GPP, R_{eco}, C_{fire}) and among land cover classes, we applied Eq. S1. We found that global NBP IAV is most strongly associated with variation in GPP; interannual GPP anomalies contribute 56% of the global NBP IAV in LPJ-GUESS, and a median of 90% in the TRENDY model ensemble. Comparing different land cover classes, the GPP anomalies of semi-arid ecosystems alone contribute 39% in LPJ-GUESS and a median of 65% in the TRENDY model ensemble to global NBP IAV (Fig. S7). Semi-arid vegetation productivity thus emerges clearly as the single most important factor governing global NBP IAV.

We employed two complementary methods to attribute the variability in GPP—as the inferred primary driver of global NBP IAV—to its environmental drivers. Firstly, we analyzed simulation results from LPJ-GUESS, linking output GPP anomalies to variability in the climatic input data. Secondly we use a time-resolved gridded global GPP product derived from upscaled flux tower measurements (*12*, *21*) (hereinafter empirical GPP product). This product uses an empirical upscaling of flux measurements and is thus entirely independent of the modelled GPP in our study.

The three main climatic drivers temperature (T), precipitation (P) and shortwave radiation (S) are interdependent and correlated. To account for combined effects of these drivers we adopt an analysis of GPP variations from an "impact perspective" (*22-24*): we first identify GPP anomalies and then extract their climatic covariates. The primary challenge of such analysis on annual scale is to target climate indices that adequately characterize the "period of climatic influence", e.g. growing season average, annual averages, minima or maxima of a given climatic forcing. To overcome this challenge we use semi-annual time series of climate drivers constructed using an optimization procedure that weights monthly anomalies of a given climate variable (T, P or S), accounting for time lags of up to 24 months while making no additional prior assumptions as to the period of influence (*12*). For each GPP event we extract climatic covariates as z-scores of the semi-annual climatic drivers.

We evaluate the climatic covariates of GPP anomalies for semi-arid ecosystems from the empirical GPP product and modelled by LPJ-GUESS, focusing on T and P, and find similar responses of GPP to climate with both approaches across all latitude bands (Fig 2 A,B). Negative GPP anomalies in semi-arid ecosystems are mainly driven by warm and dry (low rainfall) climatic events in most latitudes, suggestive of drought. By contrast, positive GPP

anomalies are dominated by cool and wet conditions. Averaging the distributions over latitudes (Fig 2 A,B) and extracting the climatic covariates per percentile of the GPP distributions shows that GPP varies with climatic conditions on a straight line in T-P space (Fig S8), with a stronger covariation with P than T. This implies that the full GPP distributions are driven by similar climatic patterns, i.e. anomalies that differ in size and sign covary with corresponding differences in size and sign in the drivers. GPP extremes (the tails of the distribution of GPP among years) covary with ENSO across all latitudes (Fig 2 C,D). Both in the model and the empirical GPP product, GPP anomalies are more strongly associated with the positive phase of ENSO (El Niño) than the negative phase (La Niña), while the sign of the relationship varies with latitude. Positive ENSO tends to coincide with negative GPP anomalies in the tropics (30°S - 20°N), and with positive GPP anomalies north of 20°N.

The agreement between climatic covariates of the data-based empirical GPP product and modelled GPP alongside the comparatively robust pattern of the covariation with climate suggests that GPP IAV for semi-arid ecosystems is mediated by climate. Since ENSO covaries with a considerable portion of the GPP distribution, we infer that ENSO is the dominating mode of global circulation variations driving GPP IAV over semi-arid ecosystems. Recent modelling studies have found that extreme El Niño events could become more common under climate change (*25*), which together with an increased atmospheric demand for water associated with global warming might exacerbate the impact of El Niño events over semi-arid ecosystems and further increase the role of semi-arid regions in driving global NBP IAV (*26-28*).

We repeat the calculation of climatic covariates to simulated NBP for LPJ-GUESS and each of the TRENDY models. The resulting maps of covariates in T-P space are shown as average covariates of negative (low CO_2 uptake or CO_2 release) extremes (Fig 3 A,B) and positive (high CO_2 uptake or low CO_2 release) extremes (Fig 3 C,D). In general, semi-arid ecosystems stand out as regions in which strong CO_2 uptake events are consistently associated with cool and moist conditions, and strong CO_2 release events with warm and dry conditions. In tropical forests NBP covaries with both T and P as in semi-arid regions, but also with T alone. In high latitudes wet or warm and wet conditions lead to negative NBP extremes whereas warm and dry or dry conditions tend to lead to positive extremes, although the spatial heterogeneity of the covariates is large in this region (Fig 3).

Our approach offers detailed spatial and temporal disaggregation of drivers and responses which is important when analyzing drivers or covariates of global NBP IAV because of the high temporal and spatial variability in P (Fig S9-11). Using four upscaling levels with increasing spatial and temporal disaggregation (ranging from land surface mean P and T to using semi-annual P and T, averaged based on the spatial origin of each year's global NBP anomaly (Eq S5 and S6)) we show that P and NBP IAV become more correlated at higher levels of disaggregation. At the highest disaggregation level, P is almost as strongly correlated with NBP IAV as T, suggesting a strong influence of soil moisture variations on global NBP IAV (*28*). This strong increase in P correlations with disaggregation resolves an apparent conflict between the findings of the present study, and those of studies using regionally averaged drivers which emphasize the role of T in governing IAV in atmospheric CO_2 (*28-30*). For semi-arid ecosystems T correlations are slightly stronger than P correlations with NBP IAV (Fig 4B), partly due to an asymmetric distribution of P and/or an asymmetric response of NBP to P IAV (Fig S12). The correlation of tropical forest P with NBP IAV

increases when we use the semi-annual drivers, suggesting large importance of accounting for time lags and "period of climatic influence" of P variations (*12*), but P-NBP IAV correlations are still weaker than T-NBP IAV correlations (Fig 4C).

Our analysis provides evidence that semi-arid ecosystems, largely occupying low latitudes, have dominated the IAV and trend of the global land C sink over recent decades. Semi-arid regions have been the subject of relatively few targeted studies that place their importance in a global context. Our findings indicate that semi-arid regions and their ecosystems merit increased attention as a key to understanding and predicting inter-annual to decadal-scale variations in the global carbon cycle.

References and Notes

1. C. Le Quéré *et al.*, Global carbon budget 2013. *Earth Syst. Sci. Data* **6**, 235-263 (2014).
2. C. D. Keeling, T. P. Whorf, M. Wahlen, J. van der Plichtt, Interannual extremes in the rate of rise of atmospheric carbon dioxide since 1980. *Nature* **375**, 666-670 (1995).
3. C. Le Quéré *et al.*, Trends in the sources and sinks of carbon dioxide. *Nature Geoscience* **2**, 831-836 (2009).
4. A. Ahlström, G. Schurgers, A. Arneth, B. Smith, Robustness and uncertainty in terrestrial ecosystem carbon response to CMIP5 climate change projections. *Environmental Research Letters* **7**, 044008 (2012).
5. P. Friedlingstein *et al.*, Climate–Carbon Cycle Feedback Analysis: Results from the C4MIP Model Intercomparison. *Journal of Climate* **19**, 3337-3353 (2006).
6. A. D. McGuire *et al.*, Carbon balance of the terrestrial biosphere in the Twentieth Century: Analyses of CO_2, climate and land use effects with four process-based ecosystem models. *Global Biogeochem. Cycles* **15**, 183-206 (2001).
7. S. Schaphoff *et al.*, Terrestrial biosphere carbon storage under alternative climate projections. *Climatic Change* **74**, 97-122 (2006).
8. S. Sitch *et al.*, Evaluation of the terrestrial carbon cycle, future plant geography and climate-carbon cycle feedbacks using five Dynamic Global Vegetation Models (DGVMs). *Global Change Biology* **14**, 2015-2039 (2008).
9. Y. Pan *et al.*, A Large and Persistent Carbon Sink in the World's Forests. *Science* **333**, 988-993 (2011).
10. A. Ahlström, P. A. Miller, B. Smith, Too early to infer a global NPP decline since 2000. *Geophys. Res. Lett.* **39**, L15403 (2012).
11. B. Smith, I. C. Prentice, M. T. Sykes, Representation of vegetation dynamics in the modelling of terrestrial ecosystems: comparing two contrasting approaches within European climate space. *Global Ecology and Biogeography* **10**, 621-637 (2001).
12. Materials and methods are available as supplementary materials on *Science* Online.
13. I. Harris, P. D. Jones, T. J. Osborn, D. H. Lister, Updated high-resolution grids of monthly climatic observations – the CRU TS3.10 Dataset. *International Journal of Climatology* **34**, 623-642 (2014).
14. G. Hurtt *et al.*, Harmonization of land-use scenarios for the period 1500–2100: 600 years of global gridded annual land-use transitions, wood harvest, and resulting secondary lands. *Climatic Change* **109**, 117-161 (2011).
15. S. Sitch *et al.*, Recent trends and drivers of regional sources and sinks of carbon dioxide. *Biogeosciences* **12**, 653-679 (2015).
16. M. A. Friedl *et al.*, MODIS Collection 5 global land cover: Algorithm refinements and characterization of new datasets. *Remote Sensing of Environment* **114**, 168-182 (2010).

17. N. Andela *et al.*, Global changes in dryland vegetation dynamics (1988–2008) assessed by satellite remote sensing: comparing a new passive microwave vegetation density record with reflective greenness data. *Biogeosciences* **10**, 6657-6676 (2013).
18. R. J. Donohue, T. R. McVicar, M. L. Roderick, Climate-related trends in Australian vegetation cover as inferred from satellite observations, 1981–2006. *Global Change Biology* **15**, 1025-1039 (2009).
19. R. Fensholt *et al.*, Greenness in semi-arid areas across the globe 1981–2007 — an Earth Observing Satellite based analysis of trends and drivers. *Remote Sensing of Environment* **121**, 144-158 (2012).
20. B. Poulter *et al.*, Contribution of semi-arid ecosystems to interannual variability of the global carbon cycle. *Nature* **509**, 600-603 (2014).
21. M. Jung *et al.*, Global patterns of land-atmosphere fluxes of carbon dioxide, latent heat, and sensible heat derived from eddy covariance, satellite, and meteorological observations. *Journal of Geophysical Research: Biogeosciences* **116**, G00J07 (2011).
22. J. Zscheischler *et al.*, A few extreme events dominate global interannual variability in gross primary production. *Environmental Research Letters* **9**, 035001 (2014).
23. M. Reichstein *et al.*, Climate extremes and the carbon cycle. *Nature* **500**, 287-295 (2013).
24. M. D. Smith, An ecological perspective on extreme climatic events: a synthetic definition and framework to guide future research. *Journal of Ecology* **99**, 656-663 (2011).
25. W. Cai *et al.*, Increasing frequency of extreme El Nino events due to greenhouse warming. *Nature Clim. Change* **4**, 111-116 (2014).
26. K. E. Trenberth *et al.*, Global warming and changes in drought. *Nature Clim. Change* **4**, 17-22 (2014).
27. A. Dai, Increasing drought under global warming in observations and models. *Nature Clim. Change* **3**, 52-58 (2013).
28. X. Wang *et al.*, A two-fold increase of carbon cycle sensitivity to tropical temperature variations. *Nature* **506**, 212-215 (2014).
29. W. Wang *et al.*, Variations in atmospheric CO2 growth rates coupled with tropical temperature. *Proceedings of the National Academy of Sciences* **110**, 13061-13066 (2013).
30. P. M. Cox *et al.*, Sensitivity of tropical carbon to climate change constrained by carbon dioxide variability. *Nature* **494**, 341-344 (2013).
31. K. Wolter, M. S. Timlin, in *Proc. of the 17th Climate Diagnostics Workshop*. (1993), pp. 52-57.
32. K. Wolter, M. S. Timlin, Measuring the strength of ENSO events: How does 1997/98 rank? *Weather* **53**, 315-324 (1998).

Supplementary Materials

www.sciencemag.com
Materials and Methods
Figs. S1-S12
References (33-57)

Acknowledgments:

The MODIS MOD12C1 land cover product was obtained through the online Data Pool at the NASA Land Processes Distributed Active Archive Center (LP DAAC), USGS/Earth Resources Observation and Science (EROS) Center, Sioux Falls, South Dakota (https://lpdaac.usgs.gov/data_access). AAhl acknowledge support from The Royal Physiographic Society in Lund (Birgit and Hellmuth Hertz' Foundation), the Swedish Research Council (637-2014-6895) and the foundation for Strategic Environmental Research (MISTRA) through the Mistra-SWECIA programme. AArn acknowledges support from EC FP7 grants LUC4C (603542). AArn, MRei and BDS acknowledge support from EC FP7 EMBRACE (282672). JGC thanks the support of the Australian Climate Change Science Program. AKJ was supported by the US National Science Foundation (NSF AGS 12-43071), the US Department of Energy (DOE DE-SC0006706) and NASA LCLUC program (NASA NNX14AD94G). EK was supported by the Environmental Research and Technology Development Fund (S-10) of the Ministry of Environment of Japan. YPW was supported by CSIRO strategic research funds. NZ acknowledge support from NOAA (NA10OAR4310248 and NA09NES4400006) and NSF (AGS-1129088). This study is a contribution to the Lund Centre for Studies of Carbon Cycle and Climate Interactions (LUCCI) and the strategic research areas MERGE and BECC.

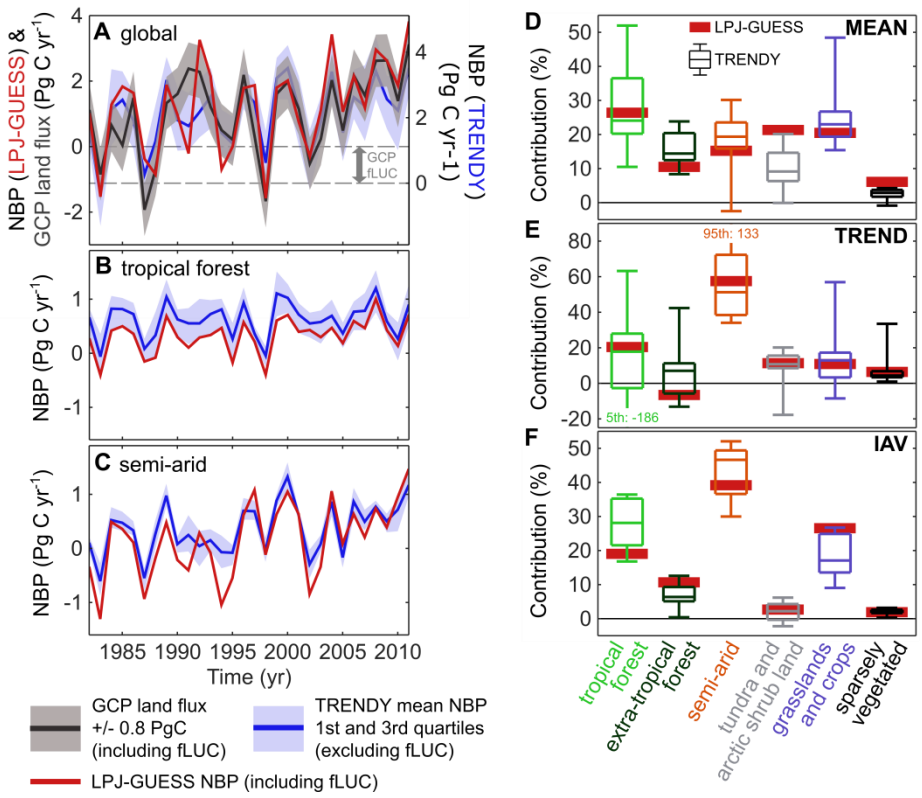

Figure 1. Global and regional NBP mean, trend and variations. (A) Global NBP and GCP land flux time series (1982 – 2011). TRENDY models are plotted on a separate vertical axis with a time-invariant offset corresponding to the time period average GCP fLUC estimate (1.2 Pg C). (B) Tropical forest NBP. LPJ-GUESS (red line) includes emissions from land use change. TRENDY models average (blue line) and 1st and 3rd quartiles of the ensemble (shaded blue area) do not include emissions from land use change. (C) NBP of semi-arid ecosystems from LPJ-GUESS (including land use change emissions) and TRENDY models (excluding land use change emissions). (D) Contribution of land cover classes to global mean NBP (1982-2011) (mean NBP of land cover class / mean global NBP). Horizontal lines in boxplots show from top, 95th, 75th, 50th, 25th, and 5th percentiles. (E) Contribution of land cover classes to global NBP trend (land cover class NBP trend / global NBP trend). (F) Contribution of land cover classes to global NBP interannual variations (Eq S1).

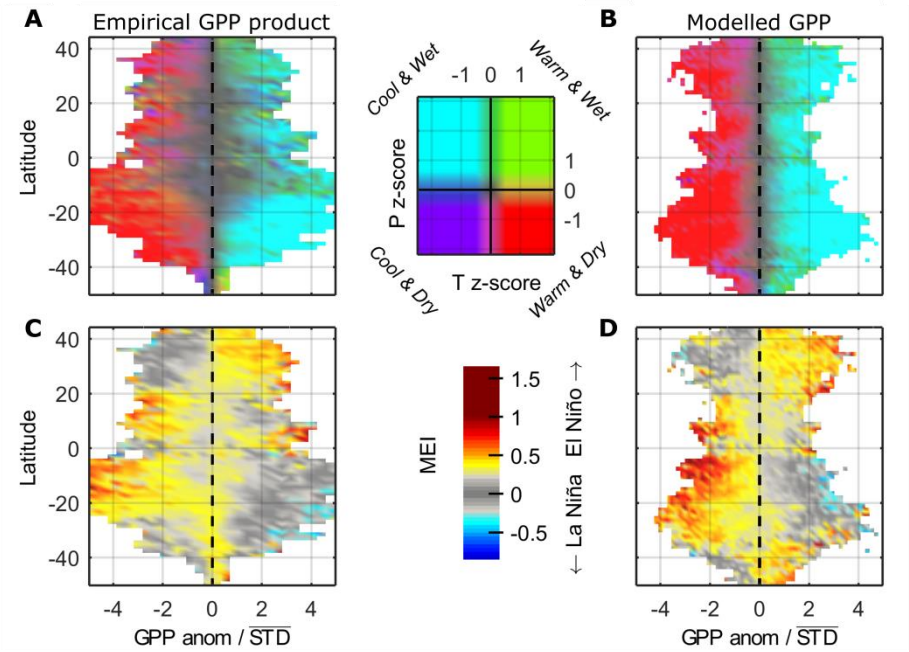

Figure 2. Climatic-covariates of semi-arid ecosystem GPP variations. (A) Distribution by latitude of the empirical GPP product anomalies normalized by average standard deviation of GPP in semi-arid lands. The distribution is colored according to the legend based on average local climatic covariates per latitude zone and distribution bin. (B) LPJ-GUESS GPP distribution calculated and colored as in (A). (C) Covariation of the multivariate ENSO index anomalies (MEI (*31*, *32*)) with the empirical GPP product. (D) Covariation of MEI and modelled GPP anomalies per latitudinal zone. NB: the figure shows the covariates of latitudinal average local GPP anomalies and not the average covariates based on GPP IAV contribution to NBP IAV.

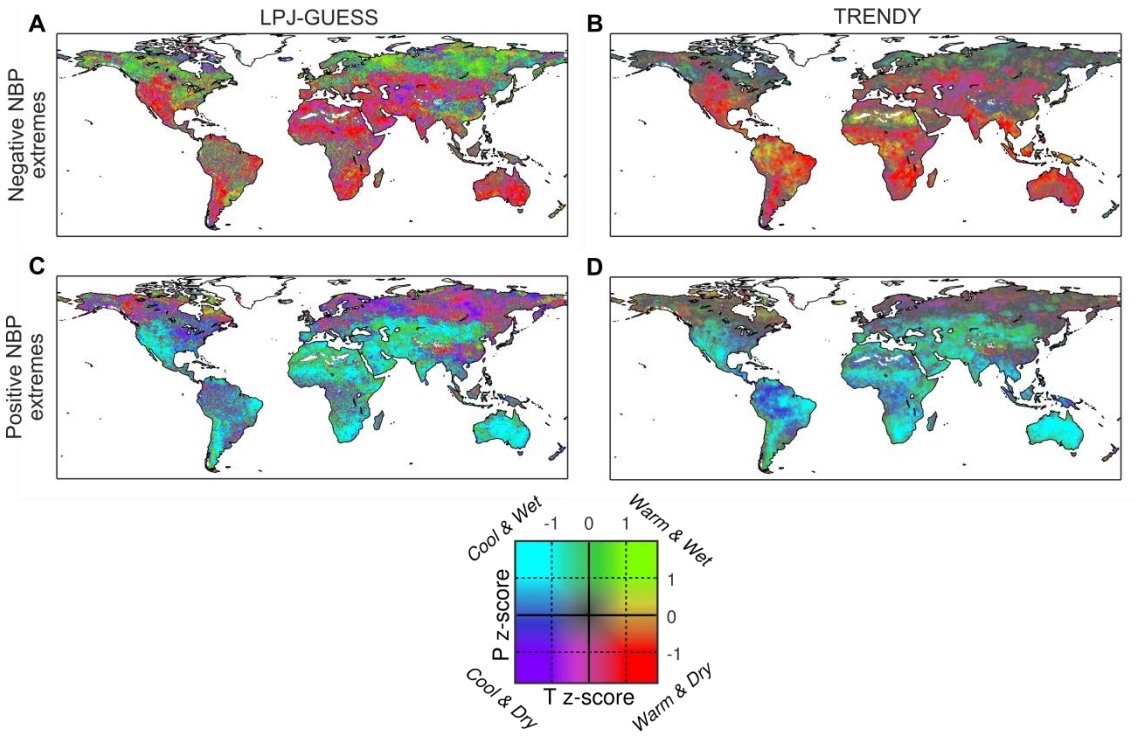

Figure 3. Climatic covariates of NBP extremes. (A) Climatic covariates of LPJ-GUESS negative NBP extremes (1-10th percentiles). (B) Mean climatic covariates of TRENDY-models negative NBP extremes (1-10th percentiles). (C) covariates of LPJ-GUESS positive NBP extremes (90-99th percentiles). (D) Mean climatic covariates of TRENDY-models positive NBP extremes (90-99th percentiles).

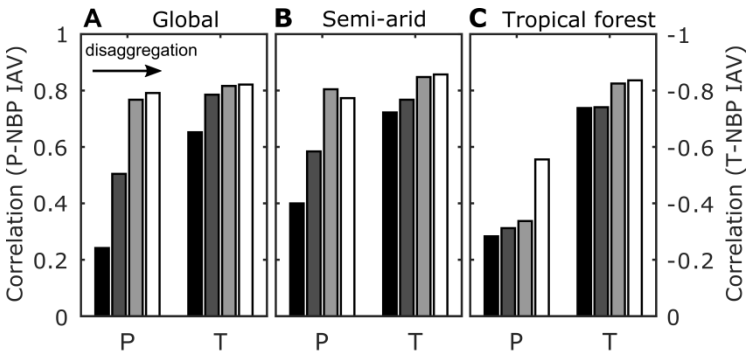

Figure 4. Correlations between annual climatic drivers IAV (P and T) and global NBP IAV (mean of all 10 models). (A) Global P and T correlations to global NBP IAV. From black to white and left to right, bars represent annual P and T IAV correlations to global NBP IAV with increasing spatial and temporal disaggregation of P and T while averaging to global time series: (I) Black bars represent averaged global land surface P and T weighted by grid cell area. (II) Dark grey bars represent P and T weighted by 30-year average contribution to global NBP IAV (Eq S1, Fig S4). (III) Light grey bars represent averaged P and T weighted by each years contributions, thus accounting for the difference in the spatial distribution of contributions between years (Eq S5 and S6). (IV) White bars represent semi-annual climate drivers averaged to global time series using the annual spatial contributions as in (III) thereby accounting for the "period of climatic influence" and time lags of up to 24 months. (B) Correlations between P and T IAV and NBP IAV for semi-arid ecosystems. Weights, where applicable, are based on contributions to global NBP IAV as in (A) but with P and T averaged over semi-arid ecosystems only. (C) Correlations between P and T IAV and global NBP IAV for tropical forest. Weights, where applicable, are based on contributions to global NBP IAV as in (A) but with P and T averaged over tropical forest only.

Supplementary Materials for

The dominant role of semi-arid ecosystems in the trend and variability of the land CO_2 sink

Anders Ahlström, Michael R. Raupach, Guy Schurgers, Benjamin Smith, Almut Arneth, Martin Jung, Markus Reichstein, Josep G. Canadell, Pierre Friedlingstein, Atul K. Jain, Etsushi Kato, Benjamin Poulter, Stephen Sitch, Benjamin D. Stocker, Nicolas Viovy, Ying Ping Wang, Andy Wiltshire, Sönke Zaehle, Ning Zeng

correspondence to: anders.ahlstrom@nateko.lu.se

This PDF file includes:

Materials and Methods

LPJ-GUESS simulations

The dynamic global vegetation model (DGVM) LPJ-GUESS (*10*, *11*) was forced by climate from CRU TS3.21 (*13*) and time-variant information on land use (*14*). LPJ-GUESS is a second-generation DGVM in which vegetation dynamics result from growth and competition for light, space and soil resources among woody plant individuals and a herbaceous understory in each of a number (100 in this study) of replicate patches in each grid cell. The patches account for the distribution within a landscape representative of the grid cell as a whole of vegetation stands with different histories of disturbance and stand development (succession). Disturbances are implemented as stochastic events with an expected frequency of 0.01 yr^{-1} at patch level. In addition, wildfires are simulated prognostically based on fuel (litter) load, dryness and physical conditions (*33*). GPP, autotrophic and heterotrophic respiration, carbon allocation and phenology, canopy gas exchange, soil hydrology and organic matter dynamics follow the approach of LPJ-DGVM (*34*, *35*). Plant functional type (PFT) settings were as described in (*10*).

TRENDY-models

The ensemble of TRENDY-model results is a combination of results for prepared for the global carbon budget of 2013 (*1*) and 2014 (*36*) through the TRENDY project, where the latest available version has been used. We use the S2 simulations where a time invariant pre-industrial land use mask (*14*) was applied (year 1860). The TRENDY model results presented here thus represent carbon cycle responses of the biophysical land surface to climate and CO_2 change, omitting emissions due to land use change or regrowth. Simulations are forced with climate information from CRU-NCEP (*37*).The ensemble consists of results from nine ecosystem models and land surface models Table S1.

Table S1. TRENDY models.

Model name	Carbon budget year	Spatial resolution (longitude x latitude)	Land surface model	Dynamic vegetation	Disturbance types	Source
CABLE	2014	0.5° x 0.5°	yes	no	-	(*38*, *39*)
ISAM	2014	0.5° x 0.5°	yes	yes	-	(*40-42*)
JULES	2014	1.875° x ~1.6°	yes	yes	-	(*43*)
LPJ	2013	0.5° x 0.5°	no	yes	fire	(*35*, *44*)
LPX	2014	1° x 1°	no	yes	fire	(*45*)
ORCHIDEE	2013	0.5°x 0.5°	yes	yes	crop harvest	(*46*)
O-CN	2013	1° x 1.2°	yes	no	-	(*47*, *48*)
VEGAS	2014	0.5° x 0.5°	yes	yes	fire	(*49*, *50*)
VISIT	2014	0.5° x 0.5°	no	no	fire, erosion	(*51*, *52*)

Empirical GPP product

The empirical GPP product originates from upscaled FLUXNET eddy-covariance tower measurements (*21*). The overall upscaling procedure involves three main steps: (I) processing and quality control of the FLUXNET data, (II) training a machine learning based regression algorithm (Model Tree Ensembles, MTEs (*53*)) for tower observed monthly GPP using site-level explanatory variables and satellite observed fraction of absorbed photosynthetic active radiation, and (III) applying the established MTEs for global upscaling, using gridded data sets of the same explanatory variables. 25 individual model trees were forced for each biosphere-atmosphere flux using gridded monthly inputs from 1982 to 2011. The best estimate of a biosphere-atmosphere flux for further analysis is the median over the 25 estimates for each pixel and month.

Half-hourly FLUXNET eddy covariance measurements were processed using standardized procedures of gap filling and quality control (*54, 55*), and the data were subsequently aggregated into monthly means. 29 explanatory variables of four types were used to train the model tree ensemble to predict biosphere-atmosphere fluxes globally (see also Table 1 in *56*), including (I) monthly fAPAR from the SeaWiFS sensor, precipitation, and temperature (both in situ measured); (II) annual changes of the fAPAR that describe properties of vegetation structure such as minimum, maximum, mean, and amplitude; (III) mean annual climate such as mean annual temperature, precipitation, sunshine hours, relative humidity, potential evapotranspiration, climatic water balance (precipitation–potential evaporation), and their seasonal dynamics; and (IV) the vegetation type according to the IGBP classification plus a flag regarding the photosynthetic pathway (C3, C4, C3/C4) (in situ information).

Land cover classes

We defined six land cover classes together covering the global land area, tropical forest, extra-tropical forest (boreal and temperate), semi-arid ecosystems, tundra and arctic shrub land, grasslands and land under agriculture (crops, here combined), and areas classified as barren (sparsely vegetated).

The global land surface was first divided into three main classes, forest, savanna and shrub lands, and grass lands and crop lands. This classification is based on a MODIS land cover classification (MCD12C1, type3) from satellite borne remote sensing (*17*), remapped using a majority filter to a spatial resolution of 0.5x0.5°. The MODIS forest category was split to tropical and extra-tropical forest using the Köppen-Geiger climate classification system (*57*). Tropical forest are defined by the Köppen-Geiger A climate group, where mean temperature of all months over the study period (1982-2011) do not fall below 18°C. Savanna and shrub lands were divided at a natural break at latitude 45°N into semi-dry ecosystems (latitudes < 45°N) and tundra and arctic shrub lands (latitudes > 45°N).

Partitioning of interannual variations

Partitioning of IAV to regions or grid cells follow the definition of Equation S1. For a given flux (NBP or GPP, R_{eco} and C_{fire}), the contribution of the IAV of a grid cell or land cover class *j* to the global NBP IAV is defined as:

$$f_j = \frac{\sum_t \frac{x_{jt}|X_t|}{X_t}}{\sum_t |X_t|} \qquad \text{(Eq. S1)}$$

where x_{jt} is the flux anomaly (departure from a long-term trend) for land cover class *j* at time *t* (in years), and X_t is the global flux anomaly, so that $X_t = \sum_j x_{jt}$. By this definition f_j is the average relative anomaly x_{jt}/X_t for region *j*, weighted with the absolute global anomaly $|X_t|$. The definition ensures that $\sum_j f_j = 1$, but allows individual f_j to fall outside the range (0,1) if the global anomaly X_t arises from partially cancelling contributions x_{jt} from different regions or regional components.

This method is not limited to estimate the variability of a dataset but rather estimates the contributions to variations in a flux (e.g. global NBP) from its constituting fluxes (e.g. regional NBP or regional GPP, R_{eco}, C_{fire}), which depends not only on the size of the constituting fluxes anomalies but also on their phase and sign (see Fig S3 for an example). Equation S1 can be applied to all detrended datasets fulfilling the basic requirement that components sum to the global, overall, flux. Therefore it can be applied to regional NBP, where regional NBP anomalies sum to global NBP anomalies. Similarly, it can be applied to NBP components, GPP, R_{eco} and C_{fire} integrated over regions or at grid cell scale since their anomalies also sum to global NBP anomalies.

The resulting scores for a region or grid cell (f_j) represent its *contribution* to global variations. Regions or grid cells with high scores drive the overall variations while regions or grid cells with low scores contribute less. Regions or grid cells with negative scores dampen variations, the overall, global, variations would therefore be larger if these negative score regions were omitted. Maps of grid cell weights are shown in Fig S4.

Optimisation of climatic co-variates

In the first step the monthly climatic drivers (*X*) were linearly detrended by month (*Xd*) and divided by their monthly standard deviation, resulting in z-scores (*Z*) of monthly anomalies

$$z_t = \frac{Xd - \overline{Xd}}{\sigma Xd} \qquad \text{(Eq. S2)}$$

For each location/grid cell *j*, *n* (24 for precipitation and 12 temperature and shortwave radiation) parameters were determined using linear regression:

$$Y_j = b_{j1}Z_{j1} + b_{j2}Z_{j2} \ldots b_{jn}Z_{jn} + \varepsilon_j \qquad \text{(Eq. S3)}$$

where *Y* is annual z-scores of GPP or NBP anomalies from 1982 through 2011, $b_{j1\text{-}n}$ represent regression parameters of monthly climatic influence on GPP or NBP annual anomalies. The semi-annual time series (*Xsa*) contains the sum of the products of the original climate variables and the normalized absolute regression parameters:

$$Xs_{jt} = \sum_i \left(\frac{|b_{ji}|}{\sum_i b_{ji}}\right) X_{jit} \qquad \text{(Eq. S4)}$$

where *i* represent the 12-24 months, and *t* years between 1982 and 2011. The monthly weights $\left(\frac{|b_i|}{\sum_i b_i}\right)$ represent the influence of the 12-24 months of climate variations on annual GPP variations.

The MEI ENSO index (*31, 32*) was optimized for time lags similarly to the climatic covariates (n=24) with the differences that it was not detrended nor standardized to z-scores. Because MEI is an index of ENSO, and therefore not spatially distributed, the same time series is used for all locations, but the monthly weights differ between locations.

Spatial and temporal weighting of P and T

In the correlation analysis of P and T IAV and global NBP IAV we average P and T globally using four methods with increasing spatial and temporal disaggregation.

(I) Annual grid cell P and T are weighted by their area.

(II) Annual grid cell P and T are weighted by their 30-year average contribution to global NBP IAV (Eq S1, Fig S4).

(III) Annual grid cell P and T are weighted each year (1982-2011) by the positive contribution of a grid cell NBP anomaly (*NBPa*) to that years global NBP anomaly (*NBPga*):

$$Cp_{jy} = max\left(\frac{NBPa_{jy}}{NBPga_y}, 0\right) \qquad \text{(Eq. S5)}$$

where *Cp* is the positive contribution of an NBP anomaly in grid cell *j* for year *y*. The weights (*W*) used for averaging are found by normalizing the positive grid cell contributions to unity:

$$W_{jy} = \frac{Cp_{jy}}{\sum_{j=0}^{n} Cp_{jy}} \qquad \text{(Eq. S6)}$$

where *n* is the number of grid cells globally or regionally.

(IV) Semi-annual grid cell P and T are weighted according to (III). This method thereby accounts for the spatial origin of annual global NBP anomalies and use climate optimized to target the "period of climatic influence" for P and T as well as for time lags of up to 24 months for P.

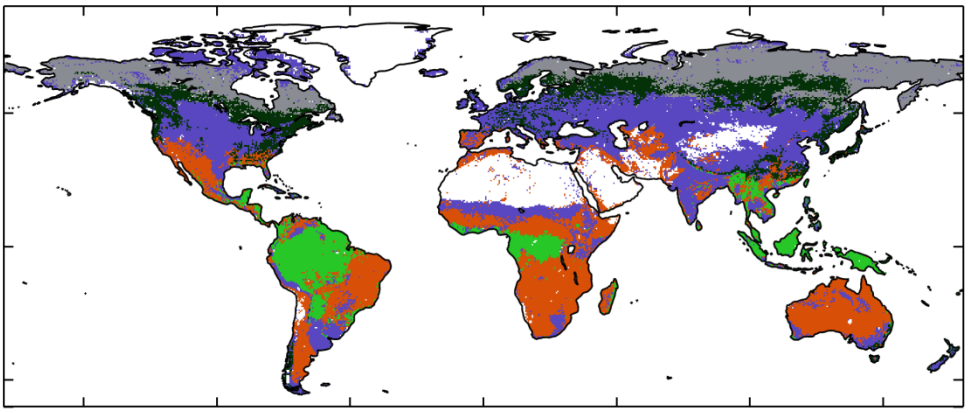

Fig. S1. Map of land cover classes. Tropical forests are shown in light green, extra-tropical forest in dark green, semi-arid ecosystems in orange, tundra and arctic shrub land in grey, grasslands and crops in blue, sparsely vegetated regions in white.

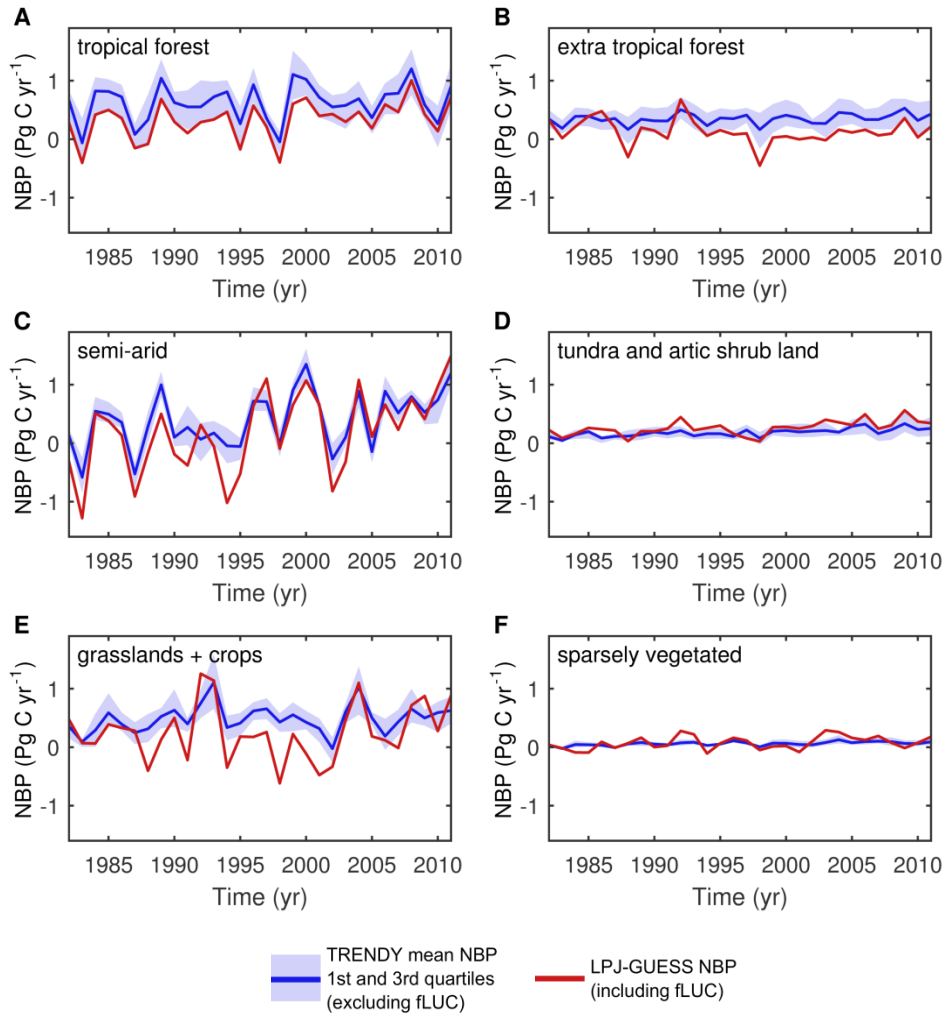

Fig. S2. NBP time-series of land cover classes from LPJ-GUESS and TRENDY-models. LPJ-GUESS accounts for emissions associated with land use change and the TRENDY-model results do not, explaining part of the difference between the two datasets. (A) NBP from LPJ-GUESS over tropical forest (red line), TRENDY-ensemble mean NBP (blue line) and 25th to 75th percentile (1st and 3rd quartiles) NBP (light blue shading). (B) Extra-tropical forest. (C) Semi-arid ecosystems. (D) Tundra and arctic shrub land. (E) Grasslands + crops. (F) Sparsely vegetated.

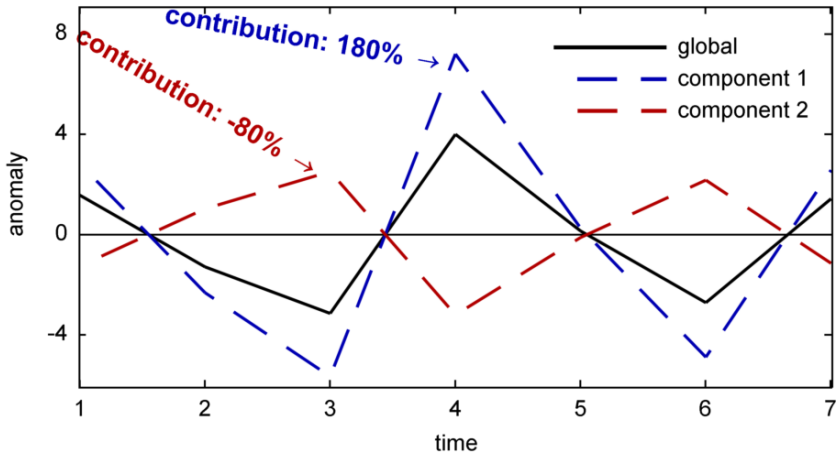

Fig. S3. Illustration of application of Equation S1. The black solid line represent a global signal and the blue and the red lines represent two components that sum to the global signal. Since component 1 varies in phase with the global signal with larger anomalies its contribution is larger than 100%, in this example, 180%. Component 2 on the other hand varies with smaller amplitude and with an opposite phase, and, since it together with component 1 sums to the global signal it must have a contribution of -80%, which would also be the result of Equation S1. Component 2 is in this example therefore dampening the global variations that would arise from only component 1.

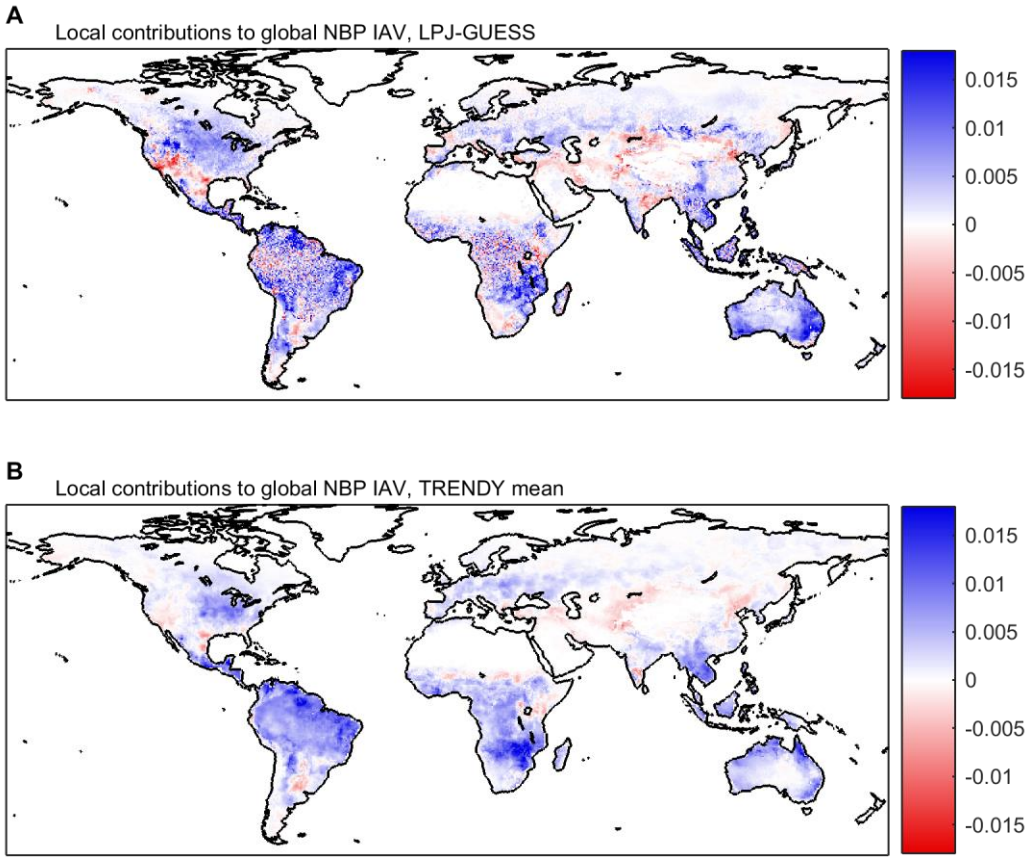

Fig. S4. Local NBP contributions to global NBP interannual variations. (A) Local NBP contributions to global NBP IAV as simulated by LPJ-GUESS (%). (B) Local NBP contributions to global NBP IAV, mean of TRENDY models (%).

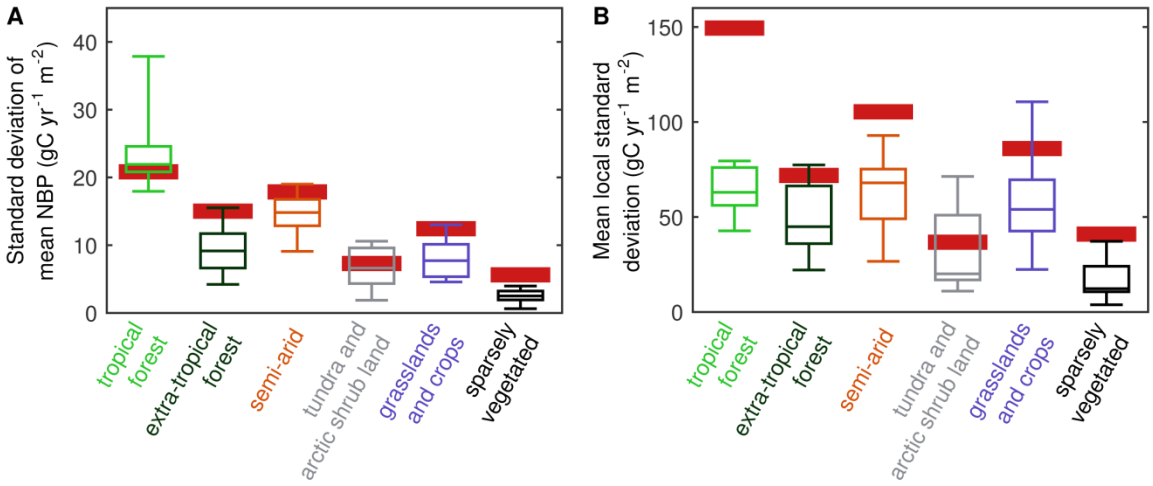

Fig. S5. Standard deviations (sd) of NBP IAV over land cover classes. (A) calculated on aggregated local NBP per land cover class; and (B) calculated for each grid cell and averaged for each land cover class. Legend as in Figure 1 (D-F). LPJ-GUESS shows higher variation among grid cells compared with TRENDY model ensemble owing mainly to stochastic representations of vegetation dynamic processes including mortality and disturbances. LPJ-GUESS sd is comparable to other models in (A) because effects of stochastic disturbances cancel between grid cells, while effects of among-grid variability are conserved in (B).
NB: the figures show local standard deviations per area unit (m^{-2}) and not contributions to global IAV. Because the variations are presented per area unit, differences in total extent between the land cover classes are not accounted for in these figures.

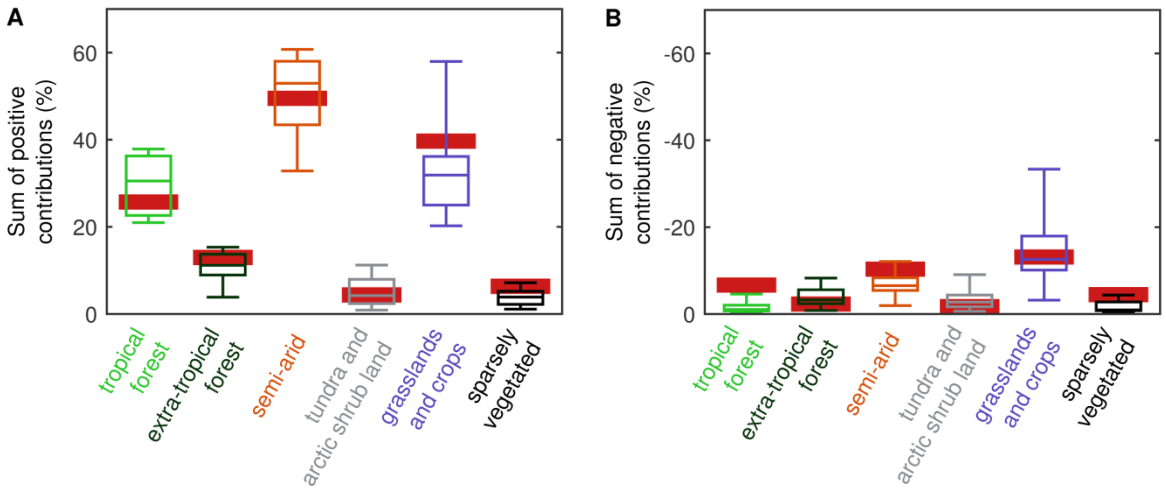

Fig. S6. Regional positive and negative NBP contributions to global NBP IAV. Panels A and B sum to the overall contribution to global NBP IAVs presented in Figure 1C. Legend as in Figure 1 (D-F). (A) Sum of positive only regional contributions to global NBP IAVs. (B) Sum of negative only regional contributions to global NBP IAV. The two panels illustrate how the contribution per land cover class could change by assessing a subset of a land cover class, e.g. dividing extra tropical forest into temperate and boreal forest. Since the overall contribution of a land cover class is the sum of local contributions, the maximum contribution of a subset of a land cover class, if all negatively contributing grid cells are removed, are shown in panel A. The relatively large negative contribution of grasslands and crops is likely due to the distribution of the land cover class across climate zones globally resulting in differences in climate variations and sensitivities to climate variations between locations.

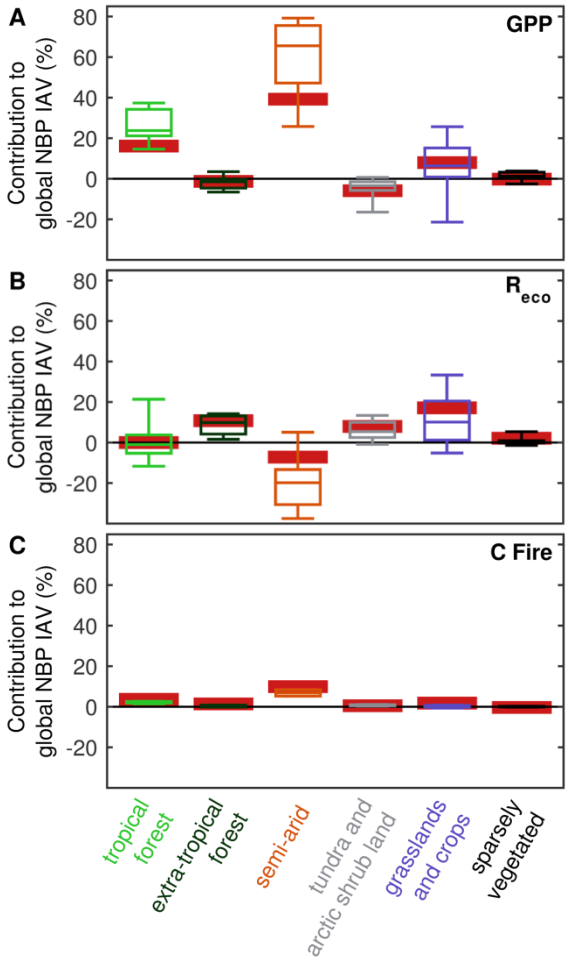

Fig. S7. Regional NBP component contributions to global NBP IAV. Legend as in Figure 1 (D-F). (A) Regional GPP contributions to global NBP IAV. (B) Regional ecosystem respiration (autotrophic + heterotrophic respiration) contributions to global NBP IAV. Decomposition of biomass residues originating from land use change is included in the LPJ-GUESS R_{eco}. (C) Regional wildfire emission (Cfire) contributions to global NBP IAV.

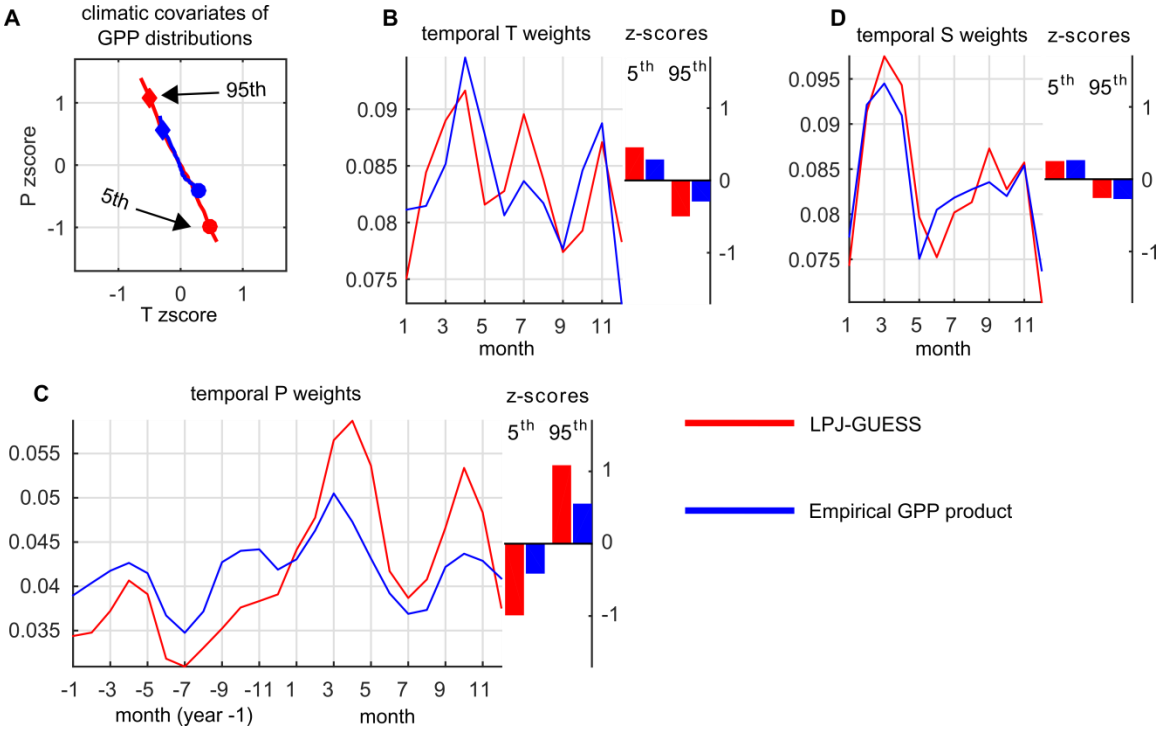

Fig. S8. Climatic covariates and temporal loadings of semi-arid ecosystems. (A) Climatic T-P space covariates of GPP percentiles 1-99 averaged over all semi-arid land weighted by grid cell area. Circles indicate the climatic covariates of the 5th percentile and diamonds indicate the 95th percentile covariates. The similar slope of the empirical GPP product and modelled GPP indicates that variations in both datasets covary with similar variations in T and P. The full distribution of both GPP datasets covary stronger with P than T; indicated by a general slope inclining towards the vertical P axis; over all percentiles of the GPP distributions, the corresponding P standardized anomaly is about twice that of the standardized T anomaly. (B) Lines indicate the monthly weights of monthly T IAV influence on GPP IAV. Bars represent the average T covariates for the 5th and 95th percentiles. (C) Lines indicate the monthly weights of monthly P IAV influence on GPP IAV. Bars represent the average P covariates for the 5th and 9th percentiles. (D) Lines indicate the monthly weights of the monthly downward shortwave radiation (S) IAV influence on GPP IAV. Bars represent the average S covariates for the 5th and 9th percentiles.

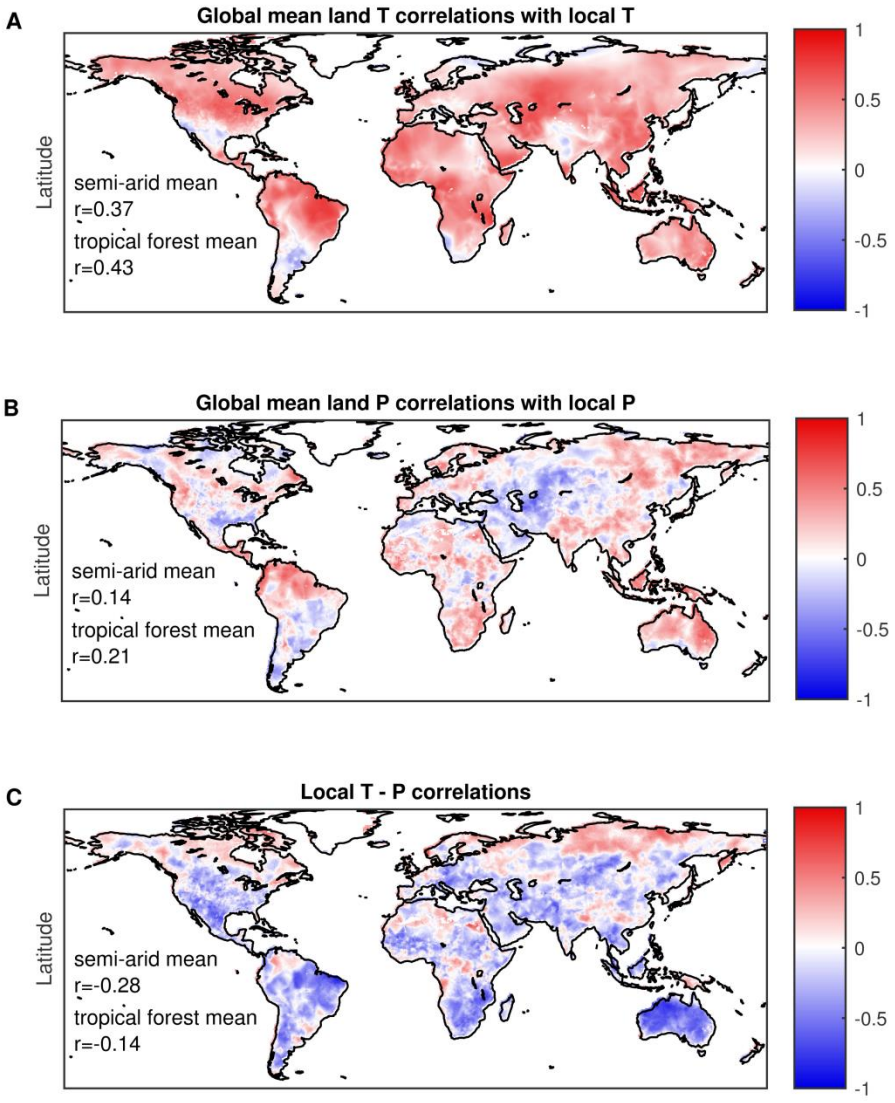

Fig. S9. Spatial properties of interannual variations of temperature and precipitation. (A) Correlations between global mean land surface temperature and local temperature interannual variations. (B) Correlations between global mean land surface precipitation and local precipitation interannual variations. (C) Local correlations between temperature and precipitation interannual variations.

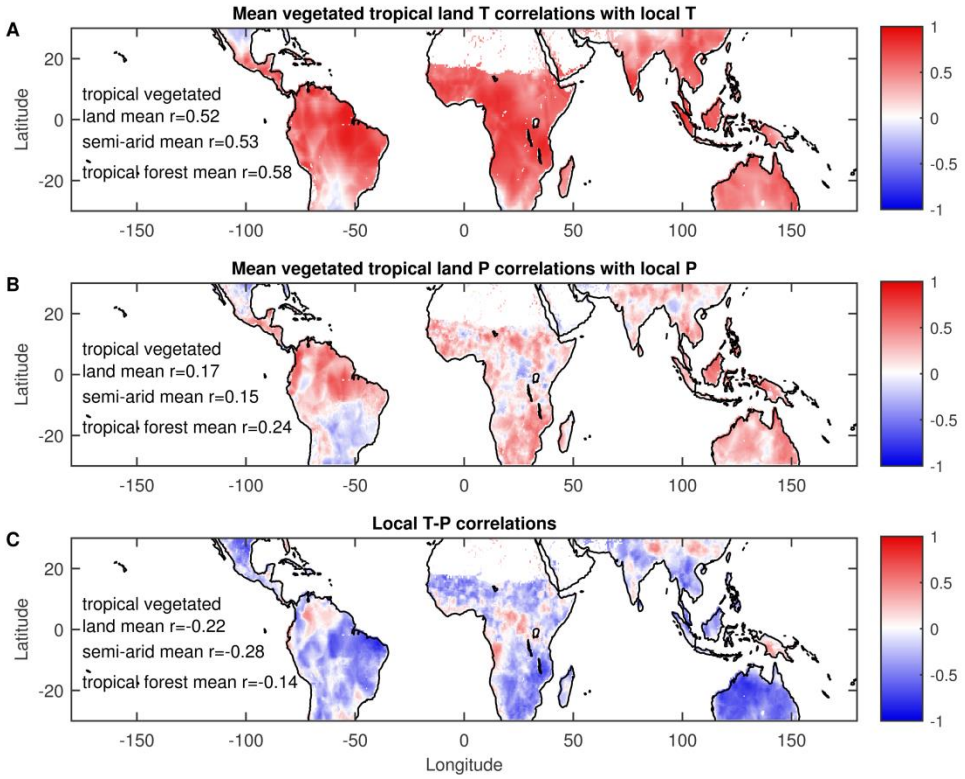

Fig. S10. Spatial properties of interannual variations of temperature and precipitation over tropical vegetated land. (A) Correlations between mean tropical vegetated land surface temperature and local temperature interannual variations. (B) Correlations between mean tropical vegetated land surface precipitation and local precipitation interannual variations. (C) Local correlations between temperature and precipitation interannual variations.

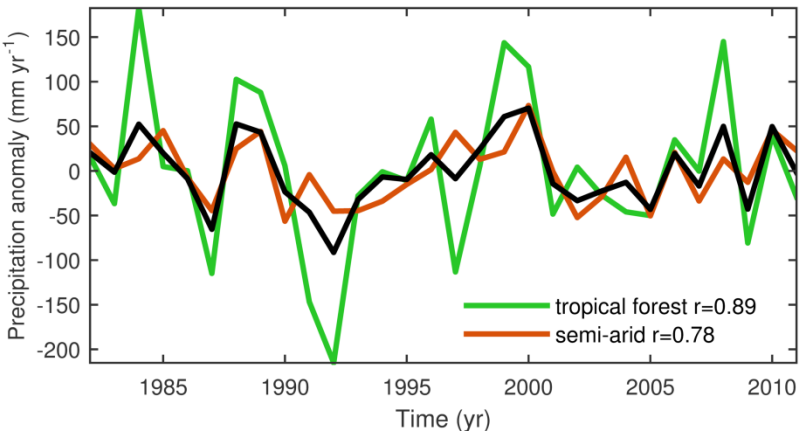

Fig. S11. Correlations between mean tropical vegetated land precipitation (black line) and tropical forest and semi-arid ecosystem interannual variations. The figure illustrates how an averaged climate signal can be affected by a region with large variations. In this example precipitation anomalies are larger over tropical forest than semi-arid ecosystems, leading to a domination of tropical forest precipitation in the aggregated time series.

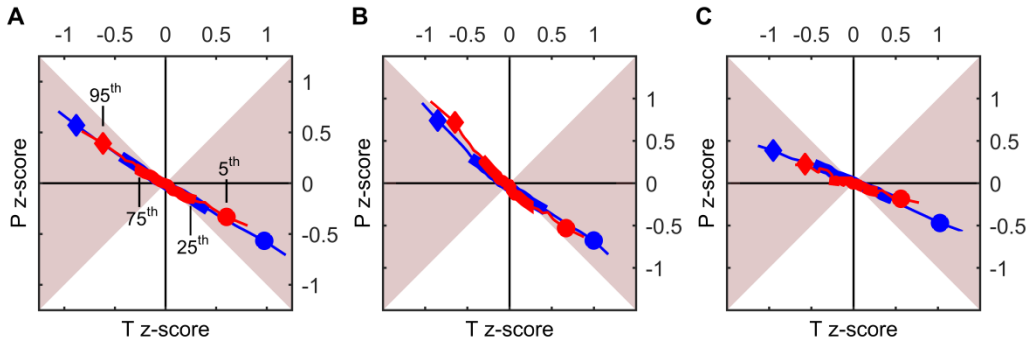

Fig. S12. Climatic covariates of contribution weighted average NBP IAV distributions. (A) Climatic covariates of global NBP IAV, spatially weighted by 30-year average contributions to global NBP IAV (Eq S1, Fig S4). LPJ-GUESS is shown in red and TRENDY-models average in blue. Shaded area illustrates where NBP covaries more with T than P, and white where NBP covaries more with P than T. (B) Climatic covariates of semi-arid ecosystems NBP IAV, spatially weighted by 30-year average contributions to global NBP IAV. Positive anomalies (percentiles >50) covaries more with P than negative anomalies due to an asymmetry in the P distribution (positive P anomalies > -negative P anomalies), and/or an asymmetrical response of NBP to P. (C) Climatic covariates of tropical forest NBP IAV, spatially weighted by 30-year average contributions to global NBP IAV.
NB: The figures show the average climatic (semi-annual) covariates of NBP IAV weighted by average contributions over 1982-2011, and is therefore not fully comparable to the correlations presented in Figure 4 at the highest level of disaggregation, where the global P and T time series are based on the spatial contributions of each year. In contrast to the correlations however, the percentile-covariation distributions shown in here are not sensitive to the non-normal distribution of P (as in (B)).

References

33. K. Thonicke, S. Venevsky, S. Sitch, W. Cramer, The role of fire disturbance for global vegetation dynamics: coupling fire into a Dynamic Global Vegetation Model. *Global Ecology and Biogeography* **10**, 661-677 (2001).
34. D. Gerten *et al.*, Terrestrial vegetation and water balance--hydrological evaluation of a dynamic global vegetation model. *Journal of Hydrology* **286**, 249-270 (2004).
35. S. Sitch *et al.*, Evaluation of ecosystem dynamics, plant geography and terrestrial carbon cycling in the LPJ dynamic global vegetation model. *Global Change Biology* **9**, 161-185 (2003).
36. C. Le Quéré *et al.*, Global carbon budget 2014. *Earth Syst. Sci. Data Discuss.* **7**, 521-610 (2014).
37. Y. Wei *et al.*, The North American Carbon Program Multi-scale Synthesis and Terrestrial Model Intercomparison Project – Part 2: Environmental driver data. *Geosci. Model Dev.* **7**, 2875-2893 (2014).
38. Y. P. Wang *et al.*, Diagnosing errors in a land surface model (CABLE) in the time and frequency domains. *Journal of Geophysical Research: Biogeosciences* **116**, G01034 (2011).
39. Y. P. Wang, R. M. Law, B. Pak, A global model of carbon, nitrogen and phosphorus cycles for the terrestrial biosphere. *Biogeosciences* **7**, 2261-2282 (2010).
40. R. Barman, A. K. Jain, M. Liang, Climate-driven uncertainties in modeling terrestrial gross primary production: a site level to global-scale analysis. *Global Change Biology* **20**, 1394-1411 (2014).
41. B. El-Masri *et al.*, Carbon dynamics in the Amazonian Basin: Integration of eddy covariance and ecophysiological data with a land surface model. *Agricultural and Forest Meteorology* **182–183**, 156-167 (2013).
42. A. K. Jain, P. Meiyappan, Y. Song, J. I. House, CO2 emissions from land-use change affected more by nitrogen cycle, than by the choice of land-cover data. *Global Change Biology* **19**, 2893-2906 (2013).
43. D. B. Clark *et al.*, The Joint UK Land Environment Simulator (JULES), model description – Part 2: Carbon fluxes and vegetation dynamics. *Geosci. Model Dev.* **4**, 701-722 (2011).
44. B. Poulter, D. C. Frank, E. L. Hodson, N. E. Zimmermann, Impacts of land cover and climate data selection on understanding terrestrial carbon dynamics and the CO2 airborne fraction. *Biogeosciences* **8**, 2027-2036 (2011).
45. B. D. Stocker *et al.*, Multiple greenhouse-gas feedbacks from the land biosphere under future climate change scenarios. *Nature Clim. Change* **3**, 666-672 (2013).
46. G. Krinner *et al.*, A dynamic global vegetation model for studies of the coupled atmosphere-biosphere system. *Global Biogeochemical Cycles* **19**, GB1015 (2005).
47. S. Zaehle, P. Ciais, A. D. Friend, V. Prieur, Carbon benefits of anthropogenic reactive nitrogen offset by nitrous oxide emissions. *Nature Geosci* **4**, 601-605 (2011).

48. S. Zaehle, A. D. Friend, Carbon and nitrogen cycle dynamics in the O-CN land surface model: 1. Model description, site-scale evaluation, and sensitivity to parameter estimates. *Global Biogeochemical Cycles* **24**, GB1005 (2010).
49. N. Zeng, Glacial-interglacial atmospheric CO2 change —The glacial burial hypothesis. *Adv. Atmos. Sci.* **20**, 677-693 (2003).
50. N. Zeng, A. Mariotti, P. Wetzel, Terrestrial mechanisms of interannual CO2 variability. *Global Biogeochemical Cycles* **19**, GB1016 (2005).
51. A. Ito, M. Inatomi, Use of a process-based model for assessing the methane budgets of global terrestrial ecosystems and evaluation of uncertainty. *Biogeosciences* **9**, 759-773 (2012).
52. E. Kato *et al.*, Evaluation of spatially explicit emission scenario of land-use change and biomass burning using a process-based biogeochemical model. *Journal of Land Use Science* **8**, 104-122 (2011).
53. M. Jung, M. Reichstein, A. Bondeau, Towards global empirical upscaling of FLUXNET eddy covariance observations: validation of a model tree ensemble approach using a biosphere model. *Biogeosciences* **6**, 2001-2013 (2009).
54. A. J. Moffat *et al.*, Comprehensive comparison of gap-filling techniques for eddy covariance net carbon fluxes. *Agricultural and Forest Meteorology* **147**, 209-232 (2007).
55. D. Papale *et al.*, Towards a standardized processing of Net Ecosystem Exchange measured with eddy covariance technique: algorithms and uncertainty estimation. *Biogeosciences* **3**, 571-583 (2006).
56. M. Jung *et al.*, Global patterns of land-atmosphere fluxes of carbon dioxide, latent heat, and sensible heat derived from eddy covariance, satellite, and meteorological observations. *Journal of geophysical Research* **16**, (2011).
57. W. Köppen, in *Handbuch der Klimatologie*, W. Köppen, R. Geiger, Eds. (Gebrüder Borntraeger, Berlin, Germany, 1936).